VNU Journal of Science: Mathematics - Physics
Journal homepage: https://js.vnu.edu.vn/MaP

Original Article

Optical, Photocatalytic and Magnetic Properties of ZnO Nanostructures Prepared by Thermal Decomposition

Kim Thi Hue My[1], Vu Xuan Son[1], Do Duc Tien[1], Nguyen Dinh Lam[1], Do Thi Huong Giang[1], Do Danh Bich[2], Luu Manh Quynh[3], Pham Duc Thang[3], Dang Ngoc Toan[4], Phan The Long[1,*]

[1]*VNU University of Engineering and Technology, 144 Xuan Thuy, Cau Giay, Hanoi, Vietnam*
[2]*Hanoi National University of Education, 136 Xuan Thuy, Cau Giay, Hanoi, Vietnam*
[3]*VNU Hanoi University of Science, 334 Nguyen Trai, Thanh Xuan, Hanoi, Vietnam*
[4]*Institute of Research and Development, Duy Tan University, Da Nang, Vietnam*

Received 5th October 2024
Revised 18th November 2024; Accepted 17th February 2025

Abstract: ZnO nanostructures have been fabricated by annealing zinc acetate dihydrate at different temperatures (T_{an}). Thermogravimetric analysis, and XRD and Raman studies indicate ZnO crystals formed at above 250 °C. An increase of T_{an} would enhance the XRD intensity and number of Raman modes characteristic of hexagonal ZnO. Below 700 °C, the samples are mainly nanorods with the diameters and lengths of 50 –100 nm and 250 – 500 nm, respectively. As T_{an} increases from 700 to 1,200 °C, nanorods transform to irregular particles with average sizes of 0.2 – 2 μm. This influences the intensity ratio of UV-to-visible emissions. Though all the samples exhibit diamagnetism, several samples with T_{an} = 500 – 700 °C have additionally weak ferromagnetic order. Assessing RhB photodegradation has demonstrated the T_{an} = 300 °C sample showing the best photocatalyticity.

Keywords: ZnO nanoparticles, thermal decomposition, optical/photocatalytic behaviors.

1. Introduction

Nanostructured materials with particle sizes smaller than 100 nm have been widely utilized in various fields of modern life, particularly in smart electronic devices, energy conversion/storage, environmental protection, healthcare and biomedical fields. Over the past decades, it has been

* Corresponding author.
E-mail address: ptlong2512@vnu.edu.vn

https//doi.org/10.25073/2588-1124/vnumap.4970

introduced numerous chemical and physical methods to synthesize and control the size, dimension, structure, and morphology of nanomaterials. Unlike counterparts in bulk, nanomaterials have the large surface-area-to-volume ratio (SAVR), and possible hetero-epitaxial growth structure. A size decrease of nanomaterials not only enhances SAVR, but also causes the quantum confinement and surface-related effects that would modify electronic/energy band structures, leading to strong electron-phonon scatterings and intriguing physicochemical properties [1-3].

Among nanomaterials, ZnO nanostructures have attracted much more especial attention from the scientific and technological community. This comes from the following facts that ZnO locates at the boundary between ionic and covalent bonds, and possesses noble physical properties. Typically, it has a high transparency, high-electron mobility, large exciton binding energy, and large bandgap energy, high thermal/mechanical stability, high piezoelectricity, and excellent photocatalyticity [4]. Apart from conventional *n*-type characters, it is possible to manufacture ZnO-based *p*-type, core/shell, flexible and ferromagnetic semiconductors [5-8]. Such characters and advantages make ZnO surpassing other oxides to become one of potential candidates suitable for many technological applications in optoelectronic/electronic devices, UV/blue lasers, nanogenerators, and biosensors [9].

Basically, nanostructured ZnO materials can be manufactured by using co-precipitation, hydrothermal synthesis, sol-gel, aqueous solution, chemical vapor deposition, and atomic layer deposition methods. Depending on techniques and fabrication conditions, various ZnO nanostructures could be facilely obtained [10, 11]. For the thermal decomposition method, though it has been widely used to prepare ZnO nanocrystals with different sizes, systematically comparative investigations about their morphological, structural, optical, magnetic and photocatalytic properties versus the annealing temperature (T_{an}) have not been carried out yet. These problems will be considered with care in the current work through experimental investigations of thermogravimetric analysis, scanning electron microscopy, X-ray diffraction, energy-dispersive X-ray spectroscopy, micro-Raman/UV-Vis/photoluminescence spectroscopy, and photocatalytic performance.

2. Experimental Details

ZnO nanostructures with nanorod- and/or irregular-shaped crystals were manufactured by the thermal decomposition method using zinc acetate dihydrate, $Zn(CH_3COO)_2{\cdot}2H_2O$ of Sigma-Aldrich® as a precursor. This chemical was taken with equal masses of ~2 g. They were loaded in uncovered alumina crucibles and in turn annealed in air for 2 h at temperatures T_{an} = 200 – 1,200 ^oC. Parallel with the annealing process, thermogravimetric analysis (TGA, Shimadzu) measurement under normal atmospheric conditions was also performed to learn about the decomposition of $Zn(CH_3COO)_2{\cdot}2H_2O$ and the formation of ZnO. After annealed at these temperatures, surface morphology and purity of the obtained products were examined by an electron microscope and an energy-dispersive X-ray spectrometer (EDS), respectively. An X-ray diffractometer (Philips X'Pert, λ = 1.5406 Å) was also employed to monitor the formation of ZnO. Micro-Raman scattering spectroscopy (XploRA PLUS, Horiba) in the backscattering model operating with an excitation wavelength (λ_{exc}) of 532 nm and the 10× optical objective was used to examine characteristic vibration modes associated with the ZnO structure. Because Raman signals of ZnO are very strong, we scanned the whole spectra for about 5 minutes. Herein Raman data presented are average values of three measurement times. Optical absorption spectra were recorded by a UV-Vis spectrophotometer (Jasco) while photoluminescent (PL) spectra were recorded by a fluorescence spectrometer (Horiba) using λ_{exc} = 325 nm from a mercury-vapor lamp (Hg lamp). Photocatalytic activity of the samples was also evaluated upon the degradation of rhodamine-B (RhB) dye under UV irradiation. In this investigation, 100 mg of each catalyst sample

was dispersed into a 200-ml solution containing 10 ppm of RhB dye, which was then stirred in dark for 10 min. The solution containing ZnO catalysts was then photocatalyzed by a UV lamp (Hg lamp), counted from 0 to 10 min. Every 2 min, an amount of the photocatalytic solution was poured out to assess RhB degradation via recording its UV-Vis absorbance after ZnO catalysts were filtered. Finally, the magnetic properties were studied through magnetic-field-dependent magnetization, $M(H)$, measurements using a vibrating sample magnetometer (Lake Shore).

3. Results and Discussion

Fig. 1 shows TGA data of zinc acetate dihydrate $Zn(CH_3COO)_2{\cdot}2H_2O$ recorded at temperatures T = 25 - 700 °C with a heating rate fixed at 10 °C/min. The variation of these data can be divided into characteristic regions. In the first region with a temperature increase from 25 to ~150 °C, about 20% initial chemical weight is reduced due to water evaporation, forming anhydrous zinc acetate - $Zn(CH_3COO)_2$. In the second range of 150 - 350 °C, a phase transition corresponding to the zinc-acetate decomposition in order to constitute ZnO is observed that causes a weight loss of ~45%. At temperatures above 350 °C, the third region, the weight loss is insignificant because the thermal stability of constituted ZnO crystals. The total weight loss owing to thermal decomposition is about 65%, corresponding to the residual ZnO product being ~35%, as shown in Fig. 1.

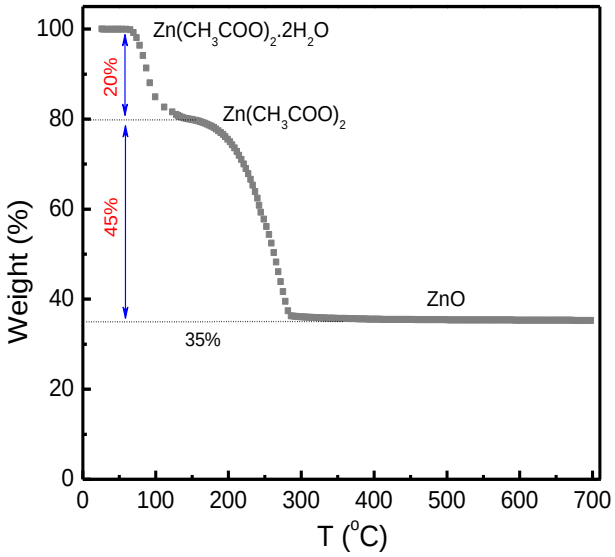

Figure 1. TGA analysis in air of zinc acetate dihydrate at temperatures T = 25~700 °C.

Employing X-ray photoelectron spectroscopy, Mar et al. [13] found that the chemical transformation of the precursor was complete at temperatures above 350 °C, and there was an incorporation of C into the samples. Based on the TGA results, we selected and annealed the samples at T_{an} = 200 - 1,200 °C, with temperature increments of 50 and 100 °C for the ranges 200~400 and 400~1,200 °C, respectively. After fabricated, particle-morphological and size changes of the samples were checked by scanning electron microscopy (SEM) under the same magnification scale. Figures 2(a-h) show SEM images of typical samples, indicating that the annealing influenced strongly the surface morphology and particle size. While the sample with T_{an} = 200 °C has an unclear resolution image, Fig. 2(a), since it mainly contains anhydrous zinc acetate, the annealing at higher temperatures constitutes particles with their

gradually increased size. At T_{an} < 700 °C, the samples are mainly nanorods with the diameters and lengths being 50~100 nm and 250~500 nm, respectively, see Figs. 2(b-d) and 2(e). When $T_{an} \geq 700$ °C, nanorods tend to change into irregular-shaped particles with the average size varying from 200 nm to ~2 μm, see Figs. 2(f-h). Those nanorods and/or irregular particles cohere together to form large clusters, especially clear grain boundaries are observed for the sample annealed at T_{an} = 1,200 °C. Herein, the morphological variation tendency observed is fairly similar to that reported by Saravanan and Katekaew et al., [14, 15]. To yield uniform nanorods, Lin et al., [12] recommended to anneal zinc acetate salts in a lid-covered alumina crucible. This could be to maintain a stable ambience for chemical reactions and ZnO-crystal development.

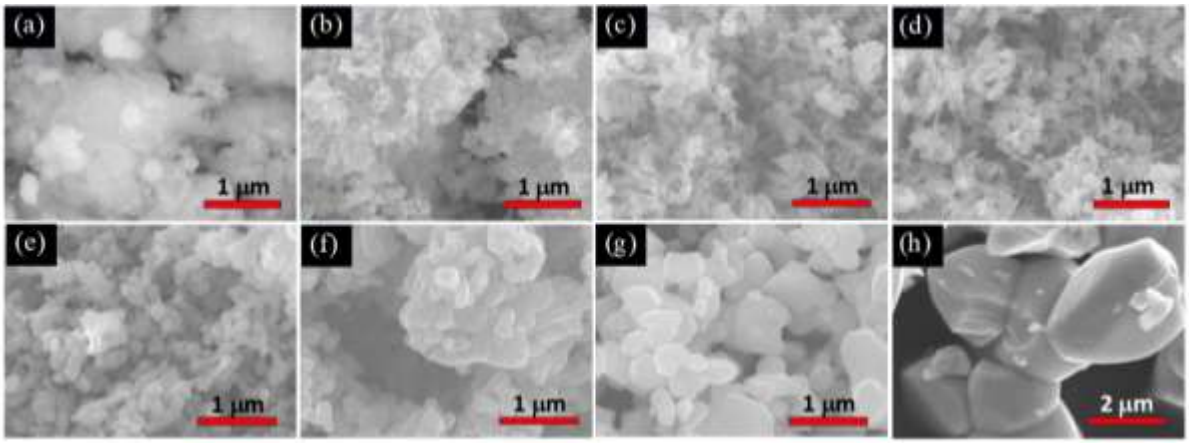

Figure 2. SEM images of the samples with T_{an} = 200 °C (a), 300 °C (b), 400 °C (c), 500 °C (d), 600 °C (e), 700 °C (f), 800 °C (g), and 1,200 °C (h).

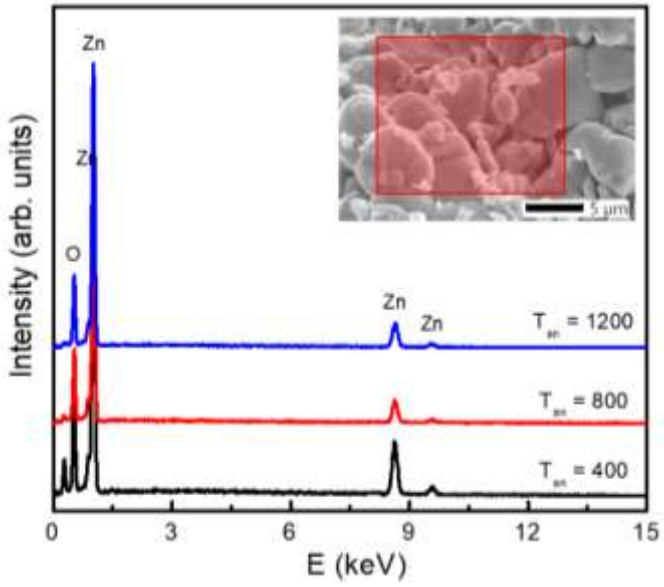

Figure 3. EDS spectra of typical samples with T_{an} = 400, 800 and 1,200 °C recorded for an inserted area.

Together with micrographs analysis, EDS spectra of representative samples with T_{an} = 400, 800 and 1,200 ºC in the energy range E = 0~15 keV were also recorded. The data graphed in Fig. 3 indicate the presence of O and Zn at ~0.52 and 8.6 keV, respectively. There is also an additional peak associated with C at the energy region below O. With the same measurement conditions, we have found a gradual decrease of the EDS-peak intensity of C when T_{an} increases, see Fig. 3. This reflects that C incorporated into ZnO samples (consistent with the results reported by Mar et al., [13]), and C content in ZnO crystals reduces as raising T_{an} to high values. Apart from this circumstance, C could be from air persisting in a vacuum chamber and absorbed on the surface of ZnO nanostructures.

We have also considered the crystal structure of the samples using the powder X-ray diffraction (XRD) technique combined with Rietveld refinement. Fig. 4 presents the XRD data of zinc acetate dihydrate annealed at different temperatures. In addition to the diffraction peaks of the initial salt, the sample annealed at T_{an} = 200 ºC displays diffraction peaks at 31.75°, 34.46°, 36.32°, 41.49°, 56.56°, 62.79°, 67.89°, and 69.04°, indicating the formation of the ZnO wurtzite/hexagonal phase (JCPDS card No. 36-1451) [7]. Having increased $T_{an} \geq$ 250 ºC, the samples exhibit only the ZnO wurtzite peaks, indicating their single-phase nature, as verified by the data refinement using the Rietveld method (Fig. 4). Another notable feature of the XRD data is the unusually high intensity of the (002) peaks, which cannot be fully described by the wurtzite phase structural model. This effect is more prominent in the samples with $T_{an} \leq$ 400 ºC and diminishes as T_{an} increases and almost disappears in the samples annealed at $T_{an} \geq$ 700 °C. It is can be attributed to the preferential orientation of nanorods developing along the *c*-axis direction [16].

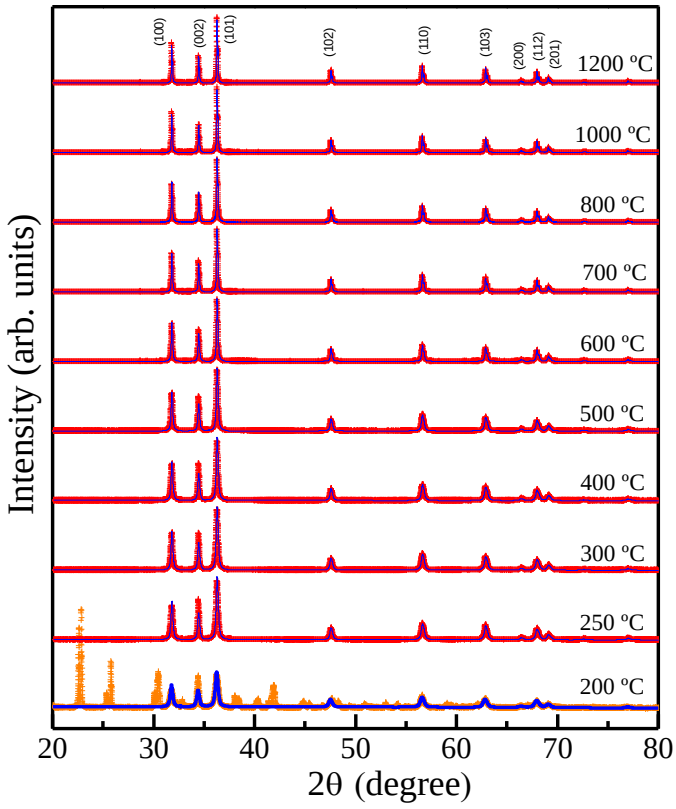

Figure 4. XRD data the samples annealed at T_{an} = 200 – 1,200 ºC. Miller-indexed peaks are from hexagonal ZnO.

Furthermore, the T_{an}-dependent variation of the unit-cell lattice parameters (a, c, c/a and V) of the ZnO wurtzite phase has been established and demonstrated in Figs. 5(a-d). These parameters exhibit opposing trends with increasing T_{an}. For $T_{an} \leq 400$ °C, the c parameter decreases sharply with increasing T_{an}, while a remains nearly unchanged. In the intermediate range 400 °C $\leq T_{an} \leq$ 700 °C, both parameters exhibit a slight decrease when T_{an} increases. Above 700 °C, the c parameter continues to decrease at a faster rate, but "a" shows a strong increase. Notably, the relative change in the c parameter $\Delta c/c$ over the experimental range of T_{an} is 0.069%, which is much larger than the 0.017% change observed for "a" parameter. The variation in the lattice parameters is reflected in an anomalous behavior of their c/a ratio and unit-cell volume. The anisotropic lattice contraction below 400 °C may be due to the annealing-induced reduction of uniaxial residual strain along the c-axis, which is typically observed in ZnO nanowires and nanorods [17, 18]. For 400 °C $\leq T_{an} \leq$ 700 °C, a similar reduction of the lattice parameters suggests that the strain in the samples becomes more isotropic. At $T_{an} \geq$ 700 °C, the opposite variation in the lattice parameters is likely related to enhanced lattice defects, as indicated by optical investigations discussed below.

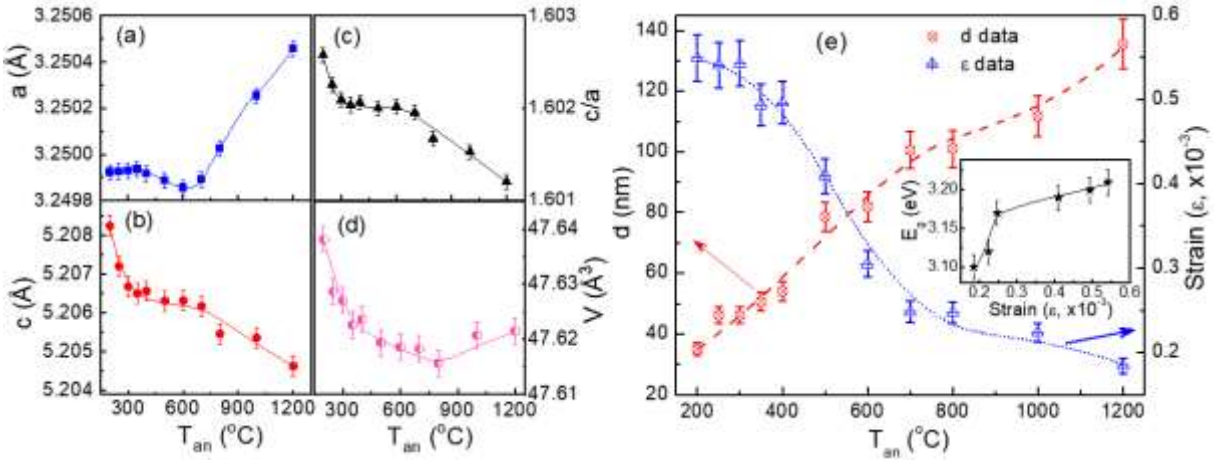

Figure 5. Structural parameters related to the hexagonal ZnO phase constituted as T_{an} = 200 – 1,200 °C: (a) a, (b) c, (c) c/a, (d) V, and (e) d and ε data dependent on T_{an}. The inset of (e) plots E_g versus ε, as discussed below.

It is necessary to add that the T_{an} raising would enhance the intensity and narrow the linewidth (β) of the XRD peaks. This is ascribed to the changes in the crystallite size (d) and lattice strain (ε) of ZnO particles. Through the Williamson-Hall approach expressed by $\beta cos\,\theta = (0.9\lambda/d) + 2\varepsilon\, sin\,\theta$, we could find the average values of both d and ε for the samples. As a function of T_{an}, their variation tendencies are opposite to each other, as graphed in Fig. 5(e). For T_{an} = 200 °C, ZnO crystals constituted in the medium of anhydrous zinc acetate have the smallest size of $d \approx 35$ nm, corresponding to the largest strain of $\varepsilon \approx 0.72\times10^{-3}$. With increasing T_{an}, d (ε) would increase (decrease) from 46 nm (0.54×10^{-3}) for T_{an} = 300 °C though ~82 nm (0.31×10^{-3}) for T_{an} = 600 °C to ~136 nm (0.18×10^{-3}) for T_{an} = 1,200 °C, see Fig. 5(e). This variation tendency of d versus T_{an} is consistent with the particle-size variation observed from SEM images. It should be noticed that d is usually smaller than the particle size determined from SEM images since their concept is totally different. Practically, to determine both d and crystallite-size distribution accurately, one can base on dark-field transmission electron microscopy.

We have additionally based on micro-Raman scattering (RS) spectroscopy to consider the development and quality of ZnO crystals generated by thermally decomposing zinc acetate dihydrate. This is an effective method to detect the mentioned things because of non-destructive and non-contact

sample manipulation. As stated by group theory, phonon modes at the Brillouin zone center of ZnO with the *P*63*mc* wurtzite-type structure include the combination [19]: $\Gamma = A_1 + 2B_1 + E_1 + 2E_2$. In this set, two B_1 modes (namely B_1(L) and B_1(H)) are silent. A_1 and E_1 are polar modes, and both Raman and infra-red active. They have longitudinal optical (LO) and transverse optical (TO) branches, in which LO-phonon frequency is strongly influenced by macroscopic electric fields generated from electromagnetic waves of excitation lasers, and dopants and/or lattice defects/distortions. Meanwhile, two non-polar modes and only Raman active of E_2(L) and E_2(H) are related to Zn- and O-sublattice vibrations, respectively [20]. Normally, these active modes are clearly observed in RS spectra of ZnO materials with a good crystal quality. Figure 6(a) shows the RS spectra of the collected samples. One can see that for the sample T_{an} = 200 °C, there are mainly unidentified modes associated with zinc acetate, with the exception of E_2(H) at ~436 cm^{-1} assigned to E_2(H) [19]. As raising T_{an} to 250 °C, vibrational modes at ~98, 330 and 382 cm^{-1} associated with E_2(L), E_2(H)-E_2(L) and A_1(TO), respectively, are activated. An increase of T_{an} to higher values, apart from the mentioned modes with stronger intensity, there is an additional appearance of conventional modes with weaker intensity peaked at ~203, 408, 579 and 658 cm^{-1} associated with 2TA [or 2E_2(L)], E_1(TO), E_1(LO) and TA+LO assignments, respectively [19]. These addressed modes have peak positions less dependent on T_{an}, and become more visible as increasing T_{an} since the single phase is attained, the quality of ZnO crystals is more and more improved. Such results are in accordance with the above XRD analysis.

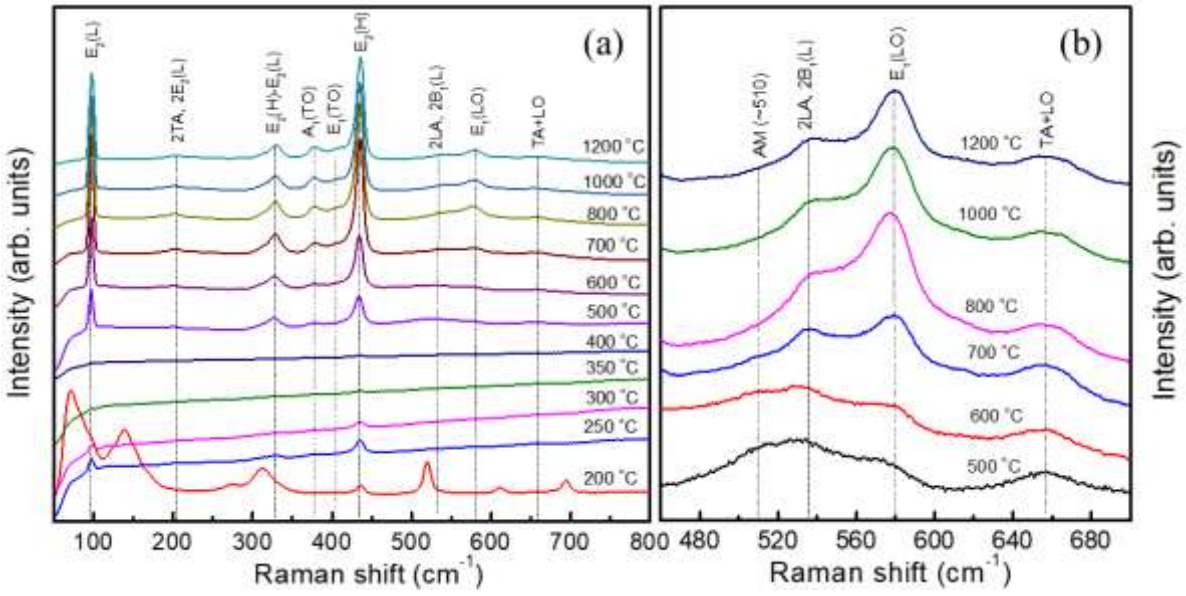

Figure 6. (a) RS spectra of the samples with T_{an} = 200 – 1,200 °C, and (b) an enlarged view of RS spectra for the samples with T_{an} = 500 – 1,200 °C in the wavenumber range of 460~700 cm^{-1}.

If more attention is given to an enlarged view of spectra at wavenumbers of 460~700 cm^{-1}, as shown in Fig. 6(b), one can see that an additional broad mode at ~536 cm^{-1} associated with 2LA [or 2B_1(L)] [19]. Interestingly, in the RS spectra of the samples with T_{an} = 500~700 °C have an anomalous mode (namely AM) peaked at ~510 cm^{-1}. Because one has found an incorporation of C into ZnO as thermally decomposing zinc acetate [13], and the AM intensity strongly decreases with increasing T_{an} above 700 °C, we believe that this mode is mainly related to C impurities, and partially to surface defects of ZnO nanoparticles (surface optical phonon vibration) [21]. As T_{an} > 700 °C, C would be burned while defects

would migrate to agglomerate together at grain boundaries, reducing the 510 cm^{-1} mode intensity (notably, the EDS-peak intensity related to C was also reduced as increasing T_{an}). The burning of C could create more lattice defects. It has been thought that E_1(LO) at 579 cm^{-1} is dependent on oxygen vacancy (V_O) content [21, 22]. More created V_O defects as increasing T_{an} could enhance the E_1(LO) intensity. Also, the A_1(LO) mode at ~560 cm^{-1} sandwiched between 2LA and E_1(LO) seems inactivate, reflecting an insignificant content of zinc interstitial (Zn_i) defects [23]. For the samples with T_{an} = 300 – 400 °C, their RS signals are too weak to possibly observe the spectral region at 460 – 700 cm^{-1}. Carefully measuring with various excitation powers, the same results and no peak shift have been still obtained. These situations prove no local heating effect, and recorded weak RS signals for T_{an} = 300 – 400 °C are related to nature of the samples. Above investigations have revealed that hydrate zinc acetate is decomposed strongly at temperatures of 300 – 400 °C. The decomposition could induce remnants, such as C, C-O, C-OH and/or $Zn_4O(CH_3CO_2)_6$ residue [12] occupying at grain boundaries and/or dislocation defects. They could absorb massively RS lights generating from ZnO, consequently weak RS signals. More studies about this issue are necessary.

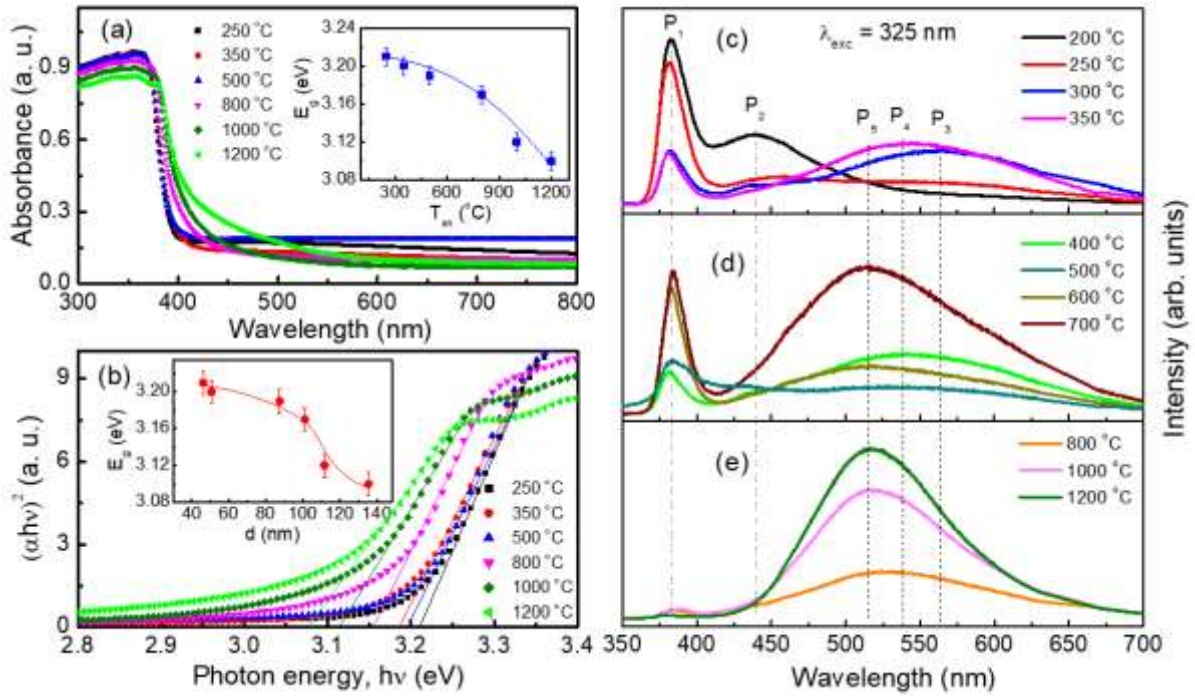

Figure 7. (a) UV-Vis spectra, (b) Tauc plots of representative ZnO samples (the insets show $E_g(T_{an})$ and $E_g(d)$ dependences), and PL spectra of the samples annealed at (c) 200~350 °C, (d) 400~700 °C and (e) 800~1,200 °C.

Clearly, above assessments have indicated ZnO materials fabricated by thermal decomposition contain intrinsic defects and C impurities. Concerning this issue, we have taken UV-Vis and PL spectra into account. Figure 7(a) shows optical absorption spectra of typical samples with different T_{an} values (≥ 250 °C). In the investigating spectral range, there is a rapid change in slope at wavelengths λ = 350 – 450 nm. It is associated with photon absorption to create electron-hole pairs, defined as the absorption edge. At temperatures $T_{an} \leq$ 500 °C, the absorption edge is less changed. However, as raising T_{an} to higher values (T_{an} > 500 °C), the redshift of this edge occurs while absorption tails at λ > 400 nm with increased signals broaden towards longer wavelengths. According to the Tauc law expressed by the

relation: $\alpha hv \propto (hv - E_g)^n$ [7], where α and hv are the absorption coefficient and excitation energy, respectively. With the direct electronic transition of ZnO, n is equal to 1/2. Based on the Tauc plots and the extrapolation of αhv to zero, as shown Fig. 7(b), we have determined E_g values of the investigated samples. The insets of Figs. 7(a, b) graph $E_g(T_{an})$ and $E_g(d)$ dependences. The results reveal the increase of T_{an} (consequently d) leading to a slight reduction of E_g from ~3.21 eV (for T_{an} = 250 ºC, d = 46.2 nm) to ~3.1 eV (for T_{an} = 1,200 ºC, d = 135.6 nm). Such inverse dependence between E_g and d is normal for ZnO nanomaterials that is usually assigned to size-related confinement effect. However, the quantum confinement effect usually appears in ZnO materials with particle sizes smaller than 10 nm. In our work, average crystallite sizes are fairly larger (d > 35 nm), reflecting that this effect is insignificant. As mentioned above, ZnO crystals in the samples with T_{an} < 500 ºC with small d values have a large strain that can enhance E_g. Additionally, C dopants present in these samples can cause doping-related degenerate, consequently widening the bandgap, known as the Burstein–Moss effect [24]. It is worth noting that UV-Vis spectra of the samples with T_{an} > 500 ºC show the Urbach absorption tail [25] broadening towards long wavelengths when T_{an} increases. Concurrently, signals nearby the absorption edge at wavelengths of ~350 nm slightly decreases. Such features hint different types of lattice defects, and their concentration varying according to T_{an}, which contribute to the bandgap narrowing effect.

Because of different defect types and their T_{an}-dependent concentration, characteristic PL spectra of the fabricated samples vary very complicatedly, see Fig. 7(c-e). Basically, the spectra consist of UV and visible emissions, and their intensity ratio varies as a function of T_{an}. For T_{an} = 200 ºC, the above analyses indicated ZnO seeds/nanocrystals embraced by hydrate zinc acetate. Its PL spectrum shows a strong UV emission (labelled as P_1) peaked at ~383 nm (3.24 eV), which is associated with the near-band-edge (NBE) emission of ZnO nanocrystals due to the radiative recombination of electrons (e^-) and holes (h^+). There is also a secondary emission (P_2) at ~439 nm (2.83 eV), probably related to the zinc acetate host lattice [26]. The P_1 emission becomes dominant while P_2 is almost invisible as T_{an} = 250 ºC when zinc acetate starts decomposing. As raising T_{an} to 300 ºC, the P_1 intensity strongly decreases while a new broad emission named P_3 appearing in the visible range peaked at ~564 nm (2.2 eV). As increasing T_{an} to 350 ºC and 400 ºC, the P_1 intensity is less changed, but the P_3 emission tends to reduces while the visible emission peak shifts to a shorter wavelength at ~539 nm (2.3 eV, named P_4), see Figs. 7(c, d). Because this T_{an} range has decomposition of zinc acetate, it is hard to identify accurately the origin of P_3 and P_4 emissions. If they are from ZnO nanocrystals only, P_3 at ~2.2 eV could be related to Zn_i-V_O [15], or V_O^{2+} that capture electrons from the conduction band (CB) [27]. Meanwhile, P_4 at 2.3 eV could be related to oxygen interstitial (O_i) that captured strongly electrons from the CB [15].

If considering the sample with T_{an} = 500 ºC, the P_1 intensity become stronger than other visible emissions (from P_1 to P_4). As increasing T_{an} from 600 to 700 ºC, the intensity of both P_1 and visible emissions increases, in which the visible emission peaked at ~515 nm (2.4 eV, named P_5) increases stronger. Such strange changes in PL-characteristic spectra of these samples (T_{an} = 500 – 700 ºC) could have the correlation with the Raman mode AM at ~510 cm^{-1} activated by C dopants and surface defects. Particularly, at higher T_{an} values (800 – 1,200 ºC), P_1 emission is rapidly reduced, while the visible one become stronger and stronger and its peak position is shifted between P_4 and P_5, belonging to the green emission (usually 2.3 – 2.5 eV), see Figs. 7(d, e). The origin of this green emission is still controversial. It could be related to oxygen antisite (O_{Zn}) [28, 29], Vo-V_{Zn} [30], O_i defects [31], and/or V_O defects [32]. We think that all mentioned Zn- and O-related defects are possible in our samples prepared by thermal decomposition. They localize in both host lattice and surface layers of ZnO particles, and tend to migrate to grain boundaries as increasing T_{an} that causes the peak shift of the green emission as observed. In general, accurate mechanisms about these emitting centers are still big challenges for research community, which warrants further study as using more state-of-the-art facilities.

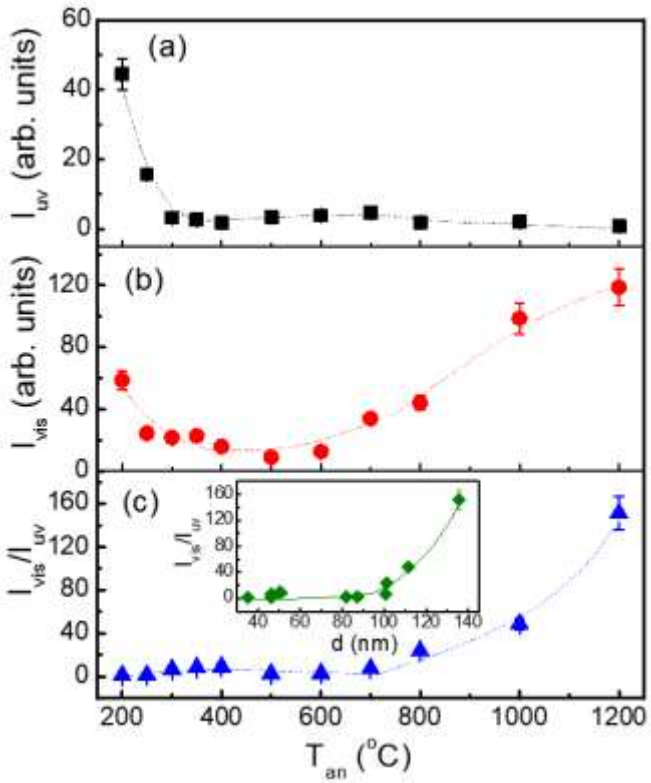

Figure 8. (a) I_{uv}, (b) I_{vis} and (c) I_{vis}/I_{uv} verus T_{an}. The inset of (c) plots I_{vis}/I_{uv} versus d data.

For a better view about PL characters of the samples as changing T_{an}, it is necessary to consider the integrated intensities of UV and visible regions, named I_{uv} and I_{vis}, respectively. The former is taken the integration in the wavelength range of 350 – 425 nm while the latter is from 425 to 700 nm. Figure 8(a, b) perform I_{uv} and I_{vis} data varying as a function of T_{an}. One can see a gradual reduction of both I_{uv} and I_{vis} when T_{an} increases from 200 to 500 °C. However, at annealing temperatures T_{an} > 500 °C, I_{uv} is less changed while I_{vis} increases with increasing T_{an}. If considering I_{vis}/I_{uv} dependent on T_{an}, Fig. 8(c), we have found that this ratio is always larger than the unity (lying in the range of 1.3 – 151.5 as T_{an} = 200 – 1,200 °C). It is less changed as T_{an} < 700 °C, but rapidly increases with increasing T_{an} to higher values (> 700 °C), which is a consequent of the d increase, as seen in the inset of Fig. 8(c). This reflects that visible emissions related to intrinsic defects are dominant in the samples with T_{an} > 700 °C. Based on the above discussion about the correlation between AM (~510 cm^{-1}) and E_1(LO) (579 cm^{-1}) modes, we think that the green emission is mainly related to V_O defects.

Together with studying optical behaviors, we have also assessed photocatalyticity of the samples with $T_{an} \geq 250$ °C. Herein, RhB dye was treated as organic pollutants and mixed with our ZnO particles with different T_{an} (d) values used as catalysts. The mixture solution was then irradiated by UV light for time (t) changing from 0 to 10 min. After ZnO catalysts were filtered, UV-Vis absorption spectra of photocatalytic solutions were checked. Figure 9(a) shows absorption spectra of RhB solutions with various t intervals, which used a representative catalyst/sample with T_{an} = 300 °C (d = 46.1 nm). For the initial spectrum (t = 0), it exhibits an absorption peak at ~555 nm. An increase of t from 2 to 10 min reduces its intensity gradually to almost zero. The decrease in absorption-peak intensity is related to the decreased RhB concentration due to photocatalytic degradation. Assume that C_0 and C_t are the initial RhB concentration (t = 0) and the RhB concentration at the irradiation time t > 0, respectively, the

degradation efficiency (*DE*) in percentage of RhB dye can be simply evaluated through the expression: $DE = [1 – (C_t/C_0)]\times100\%$ [7]. Fig 9(b). shows *DE* data of all photocatalyticity-investigated samples with T_{an} = 300 – 1,200 ºC. The results reveal the ability of RhB degradation dependent strongly on both *t* and T_{an}. Changing *t* from 0 to 10 min, the samples with T_{an} < 600 ºC show photocatalytic performance better than that of the other samples. For *t* = 10 min, their *DE* values almost achieve 100%, proving RhB molecules photodegraded effectively by UV irradiation and ZnO-nanoparticle catalysts. Meanwhile, the others have *DE* decreasing rapidly from 93% for T_{an} = 600 ºC to 36% for T_{an} = 1,200 ºC, as shown in Fig. 9(c). It means that larger sizes of ZnO particles (obtained at higher T_{an} values) would reduce remarkably photocatalytic activity.

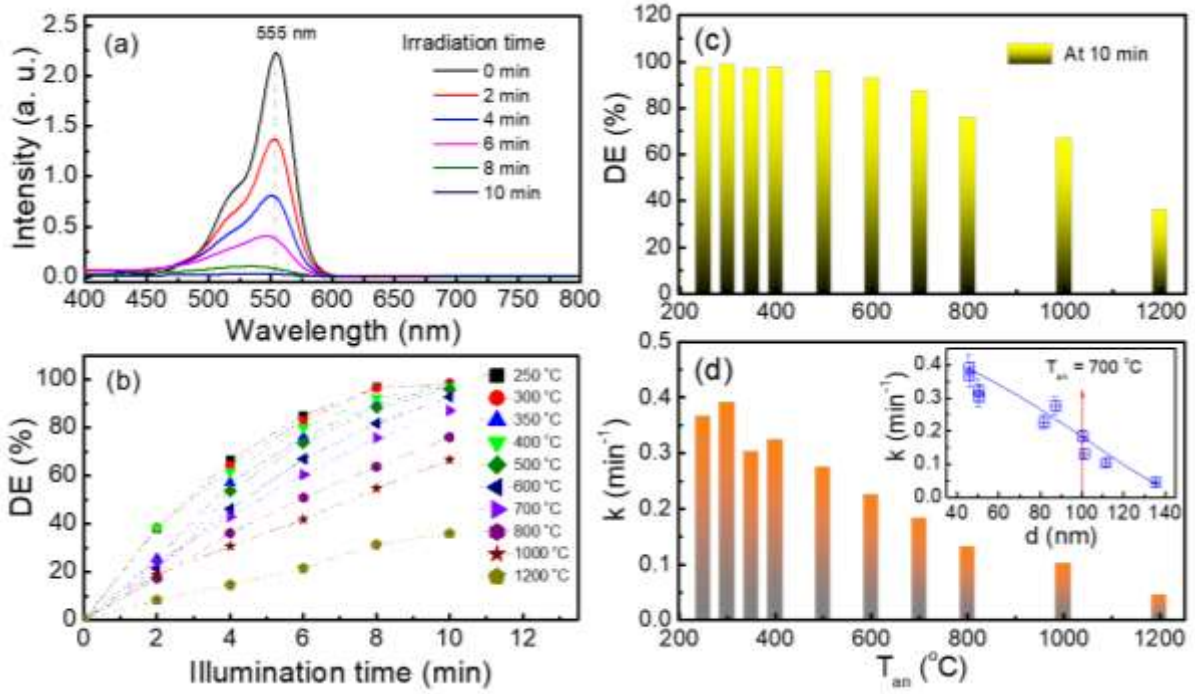

Figure 9. (a) Absorption spectra of RhB solution using ZnO catalysts (T_{an} = 300 ºC) under UV-light illumination for *t* = 0 - 10 min, (b) DE of RhB solution versus illumination time *t*, (c) DE of RhB solutions as *t* = 10 min, and (d) *d*-dependent pseudo-order rate constant *k* (in which the inset plots *d*-dependent *k* data).

It is also possible to find out the samples with good photocatalytic performance as taking photo-degradation kinetics into account. This kinetic process is usually characterized by a pseudo-rate constant (*k*) determined from the pseudo-first-order model expressed by $\ln(C_0/C_t) = kt$ [7]. Fitting experimental data of C_0/C_t *vs*. *t* to such logarithm law, we have determined *k* values. As graphed in Fig. 9(d) and its inset, *k* changes in the range of 0.05 – 0.4 and exhibits a gradual decreasing tendency when T_{an} and *d* increase. Among the investigated samples, the T_{an} = 300 ºC sample (*d* = 46.1 nm) has the largest *k* value of ~0.4 min^{-1}, meaning the best photocatalytic performance under UV-light illumination. For T_{an} = 350 – 600 ºC (*d* = 50 – 82 nm), *k* values are about 0.23~0.32 min^{-1}, which are fairly larger than those (0.15 – 0.025 min^{-1}) reported on ZnO powders prepared at 300 - 600 ºC using the same method [15, 33]. Additionally, the RhB DE of our materials achieves ~100% that takes place just ~10 min, while other works found DE being about 100% for RhB [15] and methylene blue/methyl orange [14] longer than 90 min. This could be related to different fabrication conditions and initial chemicals that influenced SAVR

and induced various lattice defects and impurities. In the current work, RS, UV-Vis absorption and PL investigations indicated many defect types (such as V_O, O_i, Zn_i, V_{Zn}, and Zn_i-V_O) and C impurities are present in the samples as changing T_{an} (d). For the samples with $T_{an} \geq 700$ °C ($d > 100$ nm), more created V_O content accompanied with other defects could massively capture UV-photoexcited carriers (e^- and h^+) that reduce the NBE emission and photocatalytic activity. Meanwhile, the samples with lower $T_{an} <$ 700 °C ($d \leq 82$ nm), their NBE emission still persists, larger SAVRs together with some active defects associated with P_3 and P_4 can contribute to an enhanced DE of RhB dye. Detailed photodegradation mechanism of RhB molecules based on ZnO catalysts and UV light can be found elsewhere [14, 15].

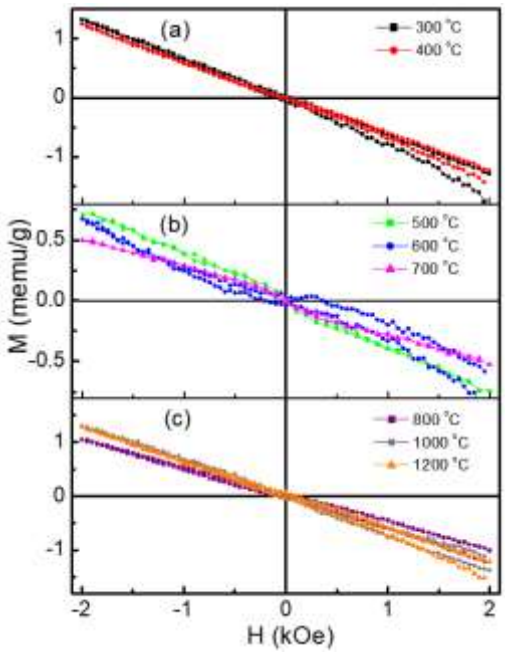

Figure 10. $M(H)$ data of the samples with T_{an} values of (a) 300 and 400 °C, (b) 500 - 700 °C, and (c) 800 – 1,200 °C.

We have also considered for magnetism in the typical samples with T_{an} = 300 – 1,200 °C through room-temperature $M(H)$ measurement. Their data graphed in Figs. 10(a-c) indicate a magnetic phase separation as changing T_{an}. Specifically, while the samples with T_{an} = 300 – 400 °C and 800 – 1,200 °C are completely diamagnetic, those with T_{an} = 500 – 700 °C have an addition of weak ferromagnetic phase besides the dominant diamagnetic phase. This causes nonlinear variation of $M(H)$ curves, particularly for T_{an} = 500 and 600 °C, see Fig. 10(b). Basically, ZnO bulk and microparticles are diamagnetic [34, 35]. However, many works have found that magnetic ordering is established when their particle size is reduced to the nanoscale, leading to the diamagnetic-ferromagnetic transition, the so-called d^0 ferromagnetism [36]. Intrinsic defects, grain boundaries, and impurities have been assigned to the origin of ferromagnetism in these materials [36, 37]. Surprisingly, in the current work, ferromagnetic ordering only appears in the samples with T_{an} = 500 – 700 °C, and becomes invisible in the $T_{an} <$ 500 °C samples with smaller d sizes and more surface defects. This reflects ferromagnetism coming from special defect types and/or impurities at their optimal concentration. If giving more attention to the RS spectral characters at T_{an} = 500 –700 °C, we believe that ferromagnetic ordering is mainly associated with the AM mode induced by C impurities. At $T_{an} <$ 500, its concentration is not optimal while at $T_{an} >$ 700 °C, its concentration is reduced by burning to create more V_O defects. These

situations are unsuitable to establish magnetic ordering. Previously, it was observed the C-induced magnetic ordering in C-doped ZnO, which is ascribed to *p-p* type interactions and spin interactions among C atoms and carriers when C substitutes oxygen to form Zn-C bonds [38].

4. Conclusion

We decomposed zinc acetate dihydrate at temperatures T_{an} = 200 – 1,200 ^{o}C to synthesize ZnO nanostructures. The results revealed that ZnO seeds forming at 200 ^{o}C. An increase of T_{an} would create more hexagonal ZnO crystals with larger crystallite sizes and better crystal quality. Concurrently, their morphology also gradually transformed from nanorods to irregular particles. Based on the Williamson-Hall method, we determined *d* changing from ~35 nm for T_{an} = 200 ^{o}C to ~136 nm for T_{an} = 1,200 ^{o}C. Particularly, the sample fabrication using thermal decomposition has been believed to create many intrinsic defect types, and C impurities. The changes in their concentration would influence RS-spectral features, the band-gap energy E_g, and the intensity of the NBE and P_1-P_5 (visible) emissions, consequently photocatalytic and magnetic behaviors. For the samples with T_{an} < 600 ^{o}C, their photocatalytic performance is better than the others ($T_{an} \geq$ 600 ^{o}C), meaning that larger sizes of ZnO particles would reduce photocatalyticity. Interestingly, the samples with T_{an} = 500 –700 ^{o}C have an existence of weak ferromagnetism besides the dominant diamagnetic phase. Based on early reported results and the AM-mode features, we believe that ferromagnetic ordering is mainly associated with C dopants present in ZnO host lattice.

Acknowledgments

This work has been supported/partly supported by VNU University of Engineering and Technology under project number CN23.09.

References

[1] Y. Chen, Y. Liu, P. Moradifar, A. J. Glaid, J. L. Russell, P. Mahale, S. Y. Yu, T. E. Culp, M. Kumar, E. D. Gomez, S. E. Mohney, T. E. Mallouk, N. Alem, J. V. Badding, Y. Liu, Quantum Transport in Three-dimensional Metalattices of Platinum Featuring an Unprecedentedly Large Surface Area to Volume Ratio, Phys. Rev. Mater., Vol. 4, 2020, pp. 035201, https://doi.org/10.1103/PhysRevMaterials.4.035201.

[2] C. K. Ghosh, Quantum Effect on Properties of Nanomaterials, in: Sengupta, A., Sarkar, C. (eds) Introduction to Nano. Engineering Materials, Springer, Berlin, Heidelberg, 2015, pp. 73-111, https://doi.org/10.1007/978-3-662-47314-6_5.

[3] K. J. Balkus, Metal Oxide Nanotube, Nanorod, and Quantum Dot Photocatalysis, in: New Futur. Dev. Catal., Elsevier, 2013, pp. 213-244, https://doi.org/10.1016/B978-0-444-53874-1.00009-3.

[4] V. Avrutin, N. Izyumskaya, Ü. Özgür, D. J. Silversmith, H. Morkoç, Ferromagnetism in ZnO- and GaN-based Diluted Magnetic Semiconductors: Achievements and Challenges, Proc. IEEE, Vol. 98, 2010, pp. 1288-1301, https://doi.org/10.1109/JPROC.2010.2044966.

[5] R. Yang, F. Wang, J. Lu, Y. Lu, B. Lu, S. Li, Z. Ye, ZnO with P-type Doping: Recent Approaches and Applications, ACS Appl. Electron. Mater., Vol. 5, 2023, pp. 4014-4034, https://doi.org/10.1021/acsaelm.3c00515.

[6] H. Jang, D. K. Kwon, D. H. Kim, J. M. Myoung, Characteristics of Flexible ZnO Nanorod UV Photodetectors Processed by Using a Direct Silicon Etching Transfer Method, J. Mater. Chem. C., Vol. 10, 2022, pp. 6805-6811, https://doi.org/10.1039/D2TC00377E.

[7] D. N. Petrov, N. T. Dang, N. D. Co, B. D. Tu, N. D. Lam, T. V. Quang, V. Q. Nguyen, J. H. Lee, B. T. Huy, D. S. Yang, D. T. Khan, T. L. Phan, Enhanced Photocatalytic Activity and Ferromagnetic Ordering in Hydrogenated $Zn_{1-x}Co_xO$, J. Mater. Sci., Vol. 59, 2024, pp. 9217-9236, https://doi.org/10.1007/s10853-024-09724-z.

[8] T. D. Pham, T. T. T. Truong, H. L. Nguyen, L. B. L. Hoang, V. P. Bui, T. T. M. Tran, T. D. Dinh, T. D. Le, Synthesis and Characterization of Novel Core–Shell $ZnO@SiO_2$ Nanoparticles and Application in Antibiotic and Bacteria Removal, ACS Omega., Vol. 7, 2022, pp. 42073-42082, https://doi.org/10.1021/acsomega.2c04226.

[9] A. K. Srivastava, J. S. Tawale, R. Verma, D. Agarwal, C. Sharma, A. Kumar, M. K. Gupta, Morphological Evolution Driven Semiconducting Nanostructures for Emerging Solar, Biological and Nanogenerator Applications, Mater. Adv., Vol. 3, 2022, pp. 8030-8062, https://doi.org/10.1039/D2MA00683A.

[10] T. L. Phan, S. C. Yu, R. Vincent, H. M. Bui, T. D. Thanh, V. D. Lam, Y. P. Lee, Influence of Mn Doping on Structural, Optical, and Magnetic Properties of $Zn_{1-x}Mn_xO$ Nanorods, J. Appl. Phys., Vol. 108, 2010, pp. 044910, https://doi.org/10.1063/1.3478709.

[11] A. A. M. Raub, R. Bahru, S. N. A. M. Nashruddin, J. Yunas, A Review on Vertical Aligned Zinc Oxide Nanorods: Synthesis Methods, Properties, and Applications, J. Nanoparticle Res., Vol. 26, 2024, pp. 186, https://doi.org/10.1007/s11051-024-06098-w.

[12] C. C. Lin, Y. Y. Li, Synthesis of ZnO Nanowires by Thermal Decomposition of Zinc Acetate Dihydrate, Mater. Chem. Phys., Vol. 113, 2009, pp. 334-337, https://doi.org/10.1016/j.matchemphys.2008.07.070.

[13] G. L. Mar, P. Y. Timbrell, R. N. Lamb, Formation of Zinc Oxide Thin Films by the Thermal Decomposition of Zinc Zcetate, In: Howe, R. F., Lamb, R. N., Wandelt, K. (eds) Surface Science. Springer Proceedings in Physics, vol 73. Springer, Berlin, Heidelberg, 1993, pp. 177-192, https://doi.org/10.1007/978-3-642-84933-6_15.

[14] R. Saravanan, E. Thirumal, V .K. Gupta, V. Narayanan, A. Stephen, The Photocatalytic Activity of ZnO Prepared by Simple Thermal Decomposition Method at Various Temperatures, J. Mol. Liq., Vol. 177, 2013, pp. 394-401, https://doi.org/10.1016/j.molliq.2012.10.018.

[15] P. Katekaew, A. Prasatkhetragarn, R. Sirirak, C. Boonruang, A. Klinbumrung, Role of the Thermal Regime in the Defect Formation of Zinc Oxide Nanostructures Prepared by the Thermal Decomposition Process, Zeitschrift Für Phys. Chemie., Vol. 237, 2023, pp. 1077-1104, https://doi.org/10.1515/zpch-2023-0235.

[16] S. K. Nikhil, A. Das, M. Kumar P, M. Bhagavathiachari, R.G. Nair, Effect of Aspect Ratio of c-axis Oriented ZnO Nanorods on Photoelectrochemical Performance and Photoconversion Efficiency, Opt. Mater. (Amst)., Vol. 121, 2021, pp. 111551, https://doi.org/10.1016/j.optmat.2021.111551.

[17] A. Das, R. G. Nair, Effect of Aspect Ratio on Photocatalytic Performance of Hexagonal ZnO Nanorods, J. Alloys Compd., Vol. 817, 2020, pp. 153277, https://doi.org/10.1016/j.jallcom.2019.153277.

[18] F. C. Tsao, J. Y. Chen, C. H. Kuo, G. C. Chi, C. J. Pan, P. J. Huang, C. J. Tun, B. J. Pong, T. H. Hsueh, C. Y. Chang, S. J. Pearton, F. Ren, Residual Strain in ZnO Nanowires Grown by Catalyst-free Chemical Vapor Deposition on GaN/Sapphire (0001), Appl. Phys. Lett., Vol. 92, 2008, pp. 203110, https://doi.org/10.1063/1.2936090.

[19] R. Cuscó, E. A. Lladó, J. Ibáñez, L. Artús, J. Jiménez, B. Wang, M. J. Callahan, Temperature Dependence of Raman Scattering in ZnO, Phys. Rev. B., Vol. 75, 2007, pp. 165202, https://doi.org/10.1103/PhysRevB.75.165202.

[20] R. Zhang, P. G. Yin, N. Wang, L. Guo, Photoluminescence and Raman Scattering of ZnO Nanorods, Solid State Sci., Vol. 11, 2009, pp. 865-869, https://doi.org/10.1016/j.solidstatesciences.2008.10.016.

[21] M. Šćepanović, M. G. Brojčin, K. Vojisavljević, S. Bernik, T. Srećković, Raman Study of Structural Disorder in ZnO Nanopowders, J. Raman Spectrosc., Vol. 41, 2010, pp. 914-921, https://doi.org/10.1002/jrs.2546.

[22] V. Russo, M. Ghidelli, P. Gondoni, C. S. Casari, A. L. Bassi, Multi-wavelength Raman Scattering of Nanostructured Al-doped Zinc Oxide, J. Appl. Phys, Vol. 115, 2014, https://doi.org/10.1063/1.4866322.

[23] A. Mondal, S. Pal, A. Sarkar, T. S. Bhattacharya, S. Pal, A. Singha, S. K. Ray, P. Kumar, D. Kanjilal, D. Jana, Raman Investigation of N-implanted ZnO: Defects, Disorder and Recovery, J. Raman Spectrosc., Vol. 50, 2019, pp. 1926-1937, https://doi.org/10.1002/jrs.5732.

[24] T. L. Phan, T. A. Ho, N. T. Dang, M. C. Nguyen, V. D. Dao, Electronic Structure, Optical and Magnetic Studies of PLD-grown (Mn, P)-doped ZnO Nanocolumns at Room Temperature, J. Phys. D. Appl. Phys., Vol. 50, 2017, pp. 295002, https://doi.org/10.1088/1361-6463/aa75e5.

[25] A. Samavati, A. F. Ismail, H. Nur, Z. Othaman, M. K. Mustafa, Spectral Features and Antibacterial Properties of Cu-doped ZnO Nanoparticles Prepared by Sol-gel Method, Chinese Phys. B., Vol. 25, 2016, pp. 077803, https://doi.org/10.1088/1674-1056/25/7/077803.

[26] N. A. Martynova, S. T. Umedov, L. S. Lepnev, M. Y. Komarova, A. V. Grigorieva, Electrochemicaly Formed ZnO and Au/ZnO Opal Films, SN Appl. Sci., Vol. 2, 2020, https://doi.org/10.1007/s42452-020-2341-z.

[27] P. A. Rodnyi, K. A. Chernenko, I. D. Venevtsev, Mechanisms of ZnO Luminescence in the Visible Spectral Region, Opt. Spectrosc. Vol. 125, 2018, pp. 357-363, https://doi.org/10.1134/S0030400X18090205.

[28] B. Lin, Z. Fu, Y. Jia, Green Luminescent Center in Undoped Zinc Oxide Films Deposited on Silicon Substrates, Appl. Phys. Lett., Vol. 79, 2001, pp. 943-945, https://doi.org/10.1063/1.1394173.

[29] T. E. Murphy, K. Moazzami, J. D. Phillips, Trap-related Photoconductivity in ZnO Epilayers, J. Electron. Mater., Vol. 35, 2006, pp. 543-549, https://doi.org/10.1007/s11664-006-0097-x.

[30] Y. W. Heo, D. P. Norton, S. J. Pearton, Origin of Green Luminescence in ZnO Thin Film grown by Molecular-Beam Epitaxy, J. Appl. Phys., Vol. 98, 2005, https://doi.org/10.1063/1.2064308.

[31] F. Wen, W. Li, J. H. Moon, J. H. Kim, Hydrothermal Synthesis of ZnO:Zn with Green Emission at Low Temperature with Reduction Process, Solid State Commun., Vol. 135, 2005, pp. 34-37, https://doi.org/10.1016/j.ssc.2005.03.066.

[32] I. Musa, N. Qamhieh, S. T. Mahmoud, Synthesis and Length Dependent Photoluminescence Property of Zinc Oxide Nanorods, Results Phys., Vol. 7, 2017, pp. 3552-3556, https://doi.org/10.1016/j.rinp.2017.09.035.

[33] S. Jayswal, R. S. Moirangthem, Thermal Decomposition Route to Synthesize ZnO Nanoparticles for Photocatalytic Application, in, 2018, pp. 020023, https://doi.org/10.1063/1.5052092.

[34] E. Tóthová, M. Senna, A. Yermakov, J. Kováč, E. Dutková, M. Hegedüs, M. Kaňuchová, M. Baláž, Z. L. Bujňáková, J. Briančin, P. Makreski, Zn Source-dependent Magnetic Properties of Undoped ZnO Nanoparticles from Mechanochemically Derived Hydrozincite, J. Alloys Compd., Vol. 787, 2019, pp. 1249-1259, https://doi.org/10.1016/j.jallcom.2019.02.149.

[35] T. L. Phan, Y. D. Zhang, D. S. Yang, N. X. Nghia, T. D. Thanh, S. C. Yu, Defect-induced Ferromagnetism in ZnO Nanoparticles Prepared by Mechanical Milling, Appl. Phys. Lett., Vol. 102, 2013, pp. 072408, https://doi.org/10.1063/1.4793428.

[36] J. M. D. Coey, Ferromagnetism, Solid State Sci., Vol. 7, 2005, pp. 660-667, https://doi.org/10.1016/j.solidstatesciences.2004.11.012.

[37] B. B. Straumal, S. G. Protasova, A. A. Mazilkin, E. Goering, G. Schütz, P. B. Straumal, B. Baretzky, Ferromagnetic Behaviour of ZnO: the Role of Grain Boundaries, Beilstein J. Nanotechnol., Vol. 7, 2016, pp. 1936-1947, https://doi.org/10.3762/bjnano.7.185.

[38] W. Q. Li, J. X. Cao, J. W. Ding, X. Hu, Modulating Magnetism of ZnO:C with Vacancy and Substitution, J. Appl. Phys., Vol. 110, 2011, https://doi.org/10.1063/1.3666051.